Using the FY-3E satellite hyperspectral infrared atmospheric sounder to quantitatively monitor volcanic SO₂

Xinyu Li[1], Lin Zhu[2], Hongfu Sun[1], Jun Li[2], Ximing Lv[1], Chengli Qi[2], Huanhuan Yan[2]

[1]College of Geoscience and Surveying Engineering, China University of Mining and Technology-Beijing, Beijing 100083, China
[2]Key Laboratory of Radiometric Calibration and Validation for Environmental Satellites, National Satellite Meteorological Center (National Center for Space Weather), Beijing 100081, China

Correspondence to: Lin Zhu (zhulin@cma.gov.cn)

Abstract. The Hyperspectral Infrared Atmospheric Sounder Type II (HIRAS-II) aboard the Fengyun 3E (FY-3E) satellite provides valuable data on the vertical distribution of atmospheric states. However, effectively extracting quantitative atmospheric information from the observations is challenging due to the large number of hyperspectral sensor channels, inter-channel correlations, associated observational errors, and susceptibility of the results to influence by trace gases. This study explores the potential of FY-3E/HIRAS-II to atmospheric loadings of SO₂ from volcanic eruptions. A methodology for selecting SO₂ sensitive channels from the large number of hyperspectral channels recorded by FY-3E/HIRAS-II is presented. The methodology allows for the selection of SO₂-sensitive channels that contain similar information on variations in atmospheric temperature and water vapor for minimizing the influence of atmospheric water vapor and temperature to SO₂. A sensitivity study shows that the difference in brightness temperature between the experimentally selected SO₂ sensitive channels and the background channels efficiency removes interference signals from surface temperature, atmospheric temperature, and water vapor during SO₂ detection and inversion. A positive difference between near-surface atmospheric temperature and surface temperature enables the infrared band to capture more SO₂ information in the lower and middle layers. The efficiency of FY-3E/HIRAS-II SO₂ sensitive channels in quantitatively monitor volcanic SO₂ is demonstrated using data from the 29 April 2024 eruption of Mount Ruang in Indonesia. Using FY-3E/HIRAS-II measurements, the spatial distribution and quantitative information of volcanic SO₂ are easily observed. The channel selection can significantly enhance the computation efficiency while maintain the accuracy of SO₂ detection and retrieval, despite the large volume of data.

1 Introduction

Volcanoes pose significant threats to human populations around the world. During eruptions, they release a variety of gases (e.g., CO₂ and SO₂), liquids (e.g., H₂O and H₂SO₄), and solids (e.g., glass, minerals, and salts), with far-reaching environmental and climatic impacts (Patrick et al., 2020). Understanding the vertical distributions of these substances is essential to analyzing their atmospheric reactions (Bauduin et al., 2017).

Sulfur dioxide (SO₂) is a magmatic volatile that is critical to volcanic geochemical analysis and hazard assessment due to its low ambient concentration, high abundance in volcanic plumes, and distinct spectral characteristics (Schmidt et al., 2012). The

1991 eruption of Mount Pinatubo and the 2014 eruption of Mount Bárðarbunga are both significant volcanic SO₂ eruption events, each producing SO₂ plumes exceeding 1×10^{10} kg (Shibata & Kinoshita, 2015). The 1991 Pinatubo eruption in particular produced a plume that peaked at 40 km height, resulting in the largest atmospheric aerosol event since the 1883

35   Krakatoa eruption (Holasek et al., 1996). Similarly, the 1982 eruption of El Chichón released approximately 7.5×10^9 kg of SO₂ into the atmosphere, reaching 31 km in height (Carey & Sigurdsson, 1986). Tropospheric volcanic SO₂ and its transformation products affect the environment, human health, air quality, and the Earth's radiation balance (Gíslason et al., 2015). Hence, systematic monitoring of volcanic SO₂ emissions is essential.

Satellite radiometry offers significant advantages for this purpose, including long-term continuity and extensive spatial

40   coverage (Krueger et al., 2009). UV band sensors are limited to monitoring SO₂ from daytime eruptions due to their reflective nature. In contrast, general infrared (IR) sensors, with their broader channels, may filter out some SO₂ spectral information (Watson et al., 2004). Different techniques have been developed which make use of satellite-based broadband IR channels to detect volcanic SO₂ plume (Corradini et al., 2021; Corradini et al., 2010; Doutriaux-Boucher & Dubuisson, 2009; Prata & Kerkmann, 2007; Prata et al., 2004; Tournigand et al., 2020). It is found that the strong absorption at 7.3 μm is heavily affected

45   by low level water vapor and thus this channel is usually used to retrieve SO₂ that is high (>3 km) in the atmosphere, and hence above most of the water vapor (Taylor et al., 2018). In addition, the retrieval is also very sensitive to uncertainties on surface temperature and emissivity (Corradini et al., 2009). Meanwhile, wide spectral channels are not sensitive enough to instantaneous changes in SO₂ composition, which will increase the minimum concentration of SO₂ components that can be monitored (Carn et al., 2003). Hyperspectral IR sensors enable continuous observations with finer channel bandwidths that

50   accurately characterize and distinguish each component, thereby reducing interference from other materials (Milstein & Blackwell, 2016). Although hyperspectral IR sensors provide thousands of spectral channels, they cannot all be used simultaneously for near real-time (NIR) operations owing to unmanageable data volumes and high computational burdens (Li & Han, 2017). At the same time, substantial redundancy and correlation mean that not all channels need to be considered. In addition, the low spectral resolution of traditional multispectral sensors makes it difficult for them to distinguish many

55   important targets (Kruse, 2004) and is limited in quantitative calculations (Feng et al., 2006), thus reducing detection and retrieval accuracy.

To improve computational efficiency and detection accuracy, and to achieve rapid and accurate data acquisition require the selection of a set of channels that provide the maximum amount of information for specific applications (Chang et al., 2020). Rabier et al. (2002) proposed the "constant" iteration method for channel selection for the Infrared Atmospheric Sounding

60   Interferometer (IASI) under clear-sky conditions, which maximized the information for applications. Fourrié and Rabier (2004) selected IASI channels for cloud-sensitive regions based on entropy reduction, demonstrating the robustness of the method Gambacorta and Barnet (2013) used a physical approach to select channels based solely on their spectral characteristics, emphasizing spectral purity, avoiding redundancy, vertical sensitivity, low instrument noise, and global optimality. Lipton (2003) developed a method to select atmospheric microwave sounding channels based on the combination of each channel's

65   center frequency, bandwidth, and degrees of freedom for the signal, and considering both applicability to multiple

Atmospheric
Measurement
Techniques
Discussions

environmental conditions and providing robust retrieval performance. Noh et al. (2017) employed the channel score index to individually evaluate channels selected using a one-dimensional variational (1Dvar) assimilation method. They used entropy subtraction for a comparative study of the selected channels, significantly reducing water vapor errors in the upper troposphere. Ventress and Dudhia (2014) proposed a 1Dvar method for selecting IASI channels and compared it with the method currently

70 employed to choose channels for numerical weather prediction; their method reduced the sensitivity of the channel set to unknown spectral correlations while maintaining the same number of degrees of freedom for the signal. As information entropy iterative techniques do not consider the dynamic impacts of measurements throughout time and only account for the reduction in atmospheric state uncertainty from a single measurement, Di et al. (2022) developed an alternative approach to channel selection for the geostationary hyperspectral IR sounder by incorporating an M-index that considers temporal variations in the

75 variance of the Jacobian. The adapted algorithm improved the accuracy of water vapor profile inversion.

The Jacobian function reflects the sensitivity of the radiation measured at a given pressure level in the atmosphere to changes in substance concentration (Di et al., 2016). In this paper, we propose a channel selection method based on the Jacobian matrix for SO₂ detection and retrieval using the Infrared Hyperspectral Atmospheric Vertical Sounder Type II (HIRAS-II) instrument onboard the Fengyun 3E (FY-3E) satellite.

80 The remainder of this paper is organized as follows. Section 2 details the data, the radiative transfer principle, and the radiative transfer model employed. Section 3 outlines the methodology of utilizing the Jacobian matrix to select sensitive and background channels for SO₂ monitoring. Section 4 investigates the effects of surface temperature and near-surface air atmospheric temperature variations on SO₂, as well as the sensitivity of detecting SO₂ plumes in the preferred channels. Section 5 demonstrated a case study of Mount Ruang on the comparison of the effectiveness of SO₂ detection between the preferred

85 channels and other absorption channels. Finally, section 6 provides a summary and discussion of the main findings.

2 Model and data

2.1 Radiation transfer model

The radiation observed by instruments at the top of the atmosphere (TOA) is modulated by the physical properties of both the atmosphere and Earth's surface (Aires et al., 2002). The atmospheric radiative transfer equation is a fundamental framework

90 that governs the behavior of solar electromagnetic radiation and thermal radiation from both the atmosphere and the surface. It is crucial to analyzing radiative transfer processes and understanding atmospheric physical parameters (Seidel et al., 2010). In the absence of scattering and assuming local thermal equilibrium, the atmospheric radiative transfer equation in the IR band can be formulated as follows:

$$R = \varepsilon B_s \tau_s - \int_0^{P_s} B d\tau + (1-\varepsilon) \int_0^{P_s} B d\tau^* + 2.16 \times 10^{-5} \pi \cos\theta \times \rho_r B_r(T_{sun}) \times {\tau_s}^2 \,, \tag{1}$$

95 where R represents spectral radiation, B is the Planck function at pressure level P, τ is total atmospheric transmittance above pressure level P, ε is surface emissivity, T is the true atmospheric temperature, ρ_r is solar reflectivity, and define $\tau^* = {\tau_s}^2/\tau$,

(Li et al., 1994). Among them, subscript s represents surface skin and subscript r represents solar radiation. The term R represents the radiation reaching the satellite. The right-hand side of the equation has four components. The first is the surface emission term, which describes the radiation emitted from the surface that is transmitted through the atmosphere to the satellite.

100 The second term accounts for the upward atmospheric radiation. The third captures the contribution of downward atmospheric radiation reflected from the surface to the satellite. The fourth term represents the contribution of solar radiation to the IR band, which can be neglected here because our focus is on the mid-wave and long-wave IR regions.

To calculate the TOA radiation using Eq. (1), the atmosphere is typically discretized into multiple layers, whose average properties (e.g., temperature, pressure, and molecular species) can be determined. Radiative transfer models facilitate this by

105 allowing precise computation of radiation transmitted through atmospheric gases.

This study uses the Line-By-Line Radiative Transfer Model (LBLRTM), which is a sophisticated, vectorized model derived from Fast Atmospheric Signature Code. LBLRTM can accurately compute atmospheric fluxes and heating rates, making it well-suited to retrieving atmospheric temperature profiles and trace gas concentrations from high-resolution spectral radiance data (Clough, 1994). The input meteorological data for this model comprise six standard atmospheric profiles: the US Standard

110 Atmosphere, 1976, and profiles for mid-latitude summer, mid-latitude winter, and subarctic summer (Krueger & Minzner, 1976). These profiles provide 99 vertical levels of atmospheric parameters such as temperature, water vapor concentration, and SO_2. Additional inputs include surface temperature, satellite zenith angle, and specific spectral band information, which are essential to calculating the simulated radiance and the Jacobian matrix. Given the spectral absorption characteristics of water vapor, temperature, and SO_2 in the IR region, this study focuses on the mid- and long-wave IR bands observed by FY-

115 3E/HIRAS-II.

2.2 FY-3E/HIRAS-II data

The FY-3E meteorological satellite is the world's first civilian dawn–dusk orbiting meteorological satellite (Zhang et al., 2022). It is part of China's second-generation polar-orbiting meteorological satellite series. Launched in July 2021, it delivers global cross-spectral atmospheric temperature and humidity vertical distribution data twice daily, in the morning and evening.

120 Working at an inclination of 98.75° and altitude of 836 km, FY-3E completes 14 orbits around the Earth's poles each day, with each orbit taking ~101.5 min, thus achieving comprehensive global coverage after 14 orbits. The satellite's HIRAS-II sensor features 3053 IR channels: 834 long-wave, 1207 mid-wave, and 1012 short-wave. Its measurements span a continuous spectrum range of 648.75 to 2551.25 cm⁻¹ at a resolution of 0.625 cm⁻¹. Each infrared band contains 3 × 3 detector arrays, which simultaneously observe the target area. A complete scanning cycle of HIRAS-II lasts 8 s, the instantaneous field of view

125 (FOV) of each detector to the ground is 1.1˚, Fig.1 is a schematic diagram of the field of view (Li et al., 2023). Based on the radiometric specifications for FY-3E/HIRAS-II, the noise equivalent target brightness temperature (BT) difference (NEdT) is specified within 0.2–0.4 K for the long-wave IR band and 0.2 – 0.3 K (at 280 K) for the mid-wave IR band (Huang et al., 2023). Overall, it delivers high-resolution IR spectra of the ground–atmosphere system.

130   Table 1 Spectral parameters of FY-3E/HIRAS-II channels

IR Wave Band	Spectral Range (cm^{-1})	No. of Channels	Spectral Resolution (cm^{-1})
Long	650 – 1136 (15.38 – 8.8 μm)	781	0.625
Mid	1210 – 1750 (8.26 – 5.71 μm)	869	0.625
Short	2155 – 2550 (4.64 – 3.92 μm)	637	0.625

In practical applications, the Level 1 (L1) observation data from HIRAS-II require apodization to mitigate sidelobe effects (Xie et al., 2023). This is accomplished in the present study using the Hamming window function. In addition, radiometric measurements are typically integrated over a wavenumber interval and modified by the instrument's line shape (Crevoisier et al., 2003). Consequently, we convolve the simulated brightness temperature (BT) with the FY-3E/HIRAS-II spectral response
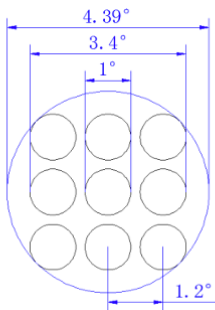
135   function to facilitate subsequent channel selection.

Figure 1: HIRAS-II detector distribution and corresponding ground field of view.

2.3 Sentinel-5P/TROPOMI SO₂ data

Sentinel-5P is a quasi-polar, sun-synchronous satellite in a low Earth orbit with a height of about 824 km, and it covers the entire planet each day. Every orbital period lasts 16 days, with an average of 227 orbits every period (14 orbits per day) (Corradino et al., 2024). The satellite hosts the Tropospheric Monitoring Instrument (TROPOMI). Daily or sub-daily revisits

140   of specific sites are achievable, given TROPOMI's 108° cross-orbit field of view and its ability to capture data across multiple orbits. Since 2019, Sentinel-5P's spatial resolution has been enhanced to 3.5 km × 5.5 km. TROPOMI measures data across four spectral regions (ultraviolet, visible, near-infrared, and shortwave infrared) and is adept at monitoring SO₂ and a range of other gases. With a comparable footprint of 12 km diameter, TROPOMI demonstrates greater sensitivity to SO₂ variations than IASI (Cofano et al., 2021).

145 This study uses TROPOMI's Level 2 (L2) geophysical SO_2 products, accessible through the European Space Agency's Copernicus Open Access Center via the Sentinel-5P Pre-Operations Hub. We are using the offline (OFFL) data of this version, which are freely available (Copernicus Sentinel-5P, 2020). These L2 products are derived from Level 0 (L0) raw data, which undergo calibration and georeferencing, followed by processing to Level 1b (L1b) data, including brightness and irradiance. In this study, Sentinel-5P/TROPOMI SO_2 data are primarily employed to validate the SO_2 detection capabilities of FY-

150 3E/HIRAS-II at Mount Ruang (Inness et al., 2022).

2.4 Atmospheric profile data

This study employs standard atmospheric profile data as inputs for the LBLRTM. The profiles used are the US Standard Atmosphere, 1976, and tropical, mid-latitude summer and winter, subarctic summer and winter profiles. The US Standard Atmosphere, 1976, serves as an idealized stable representation of Earth's atmosphere from the surface to 1000 km, detailing

155 the relative changes in atmospheric composition with altitude. Below 86 km, the atmospheric composition is calculated using a series of linear functions, while the upper region is defined by continuous functions that closely approximate observational data (Krueger & Minzner, 1976).

ERA5 is the latest comprehensive reanalysis dataset from the European Centre for Medium-Range Weather Forecasts (ECMWF), superseding ERA-Interim. With daily updates, ERA5 provides hourly estimates of the world's atmosphere, land

160 surface, and waves in the ocean from 1950 onward (Hersbach et al., 2020). Each profile from ERA5 has a horizontal scale of 31 km and 137 vertical levels, ranging from near-surface air pressure to 0.01 hPa. For this study, we interpolate ERA5 data to assess atmospheric water vapor conditions near Mount Ruang concurrent with FY-3E/HIRAS-II observations.

3 Channel selection method

When selecting channels, it is crucial to avoid bands with cloud or aerosol interference and long-wave channels that provide

165 redundant information (Tsuchiya, 1983). In addition, as the temperature Jacobian matrices of the water vapor and ozone channels can be strongly influenced by the state of the atmosphere, they should not be used as the main sources of temperature information (Kuai et al., 2010). Therefore, different sets of channels should be considered at various stages during the channel selection process. This research suggests two primary steps for channel selection, as follows.

1. Initially, channels are excluded through pre-screening, which eliminates regions of high uncertainty in the simulated

170 spectrum based on specific criteria.

2. The primary channel selection algorithm is based on Jacobian calculations as a measure of the information content of various atmospheric species and is executed through multiple independent selection operations.
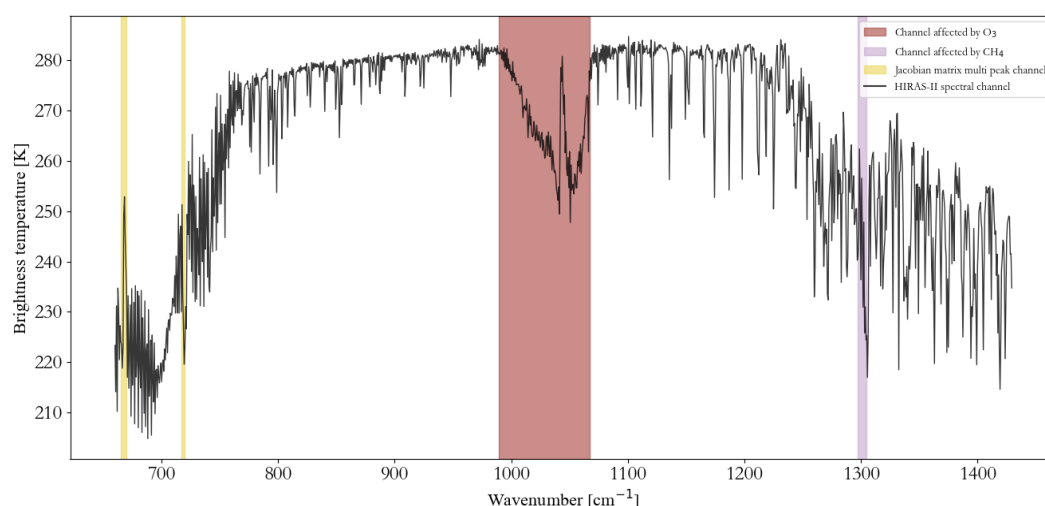
3.1 Channel pre-screening

Channel pre-screening rejects spectral regions that would bring substantial uncertainty in the subsequent simulation phase,
175   thus enhancing the efficiency of and reducing data redundancy in the forward simulations (Li et al., 2022). We pre-screened
the mid- and long-wave IR bands by eliminating trace gas absorption channels and applying a threshold to the noise equivalent
target brightness temperature (BT) difference (NEdT).

The first step eliminates channels with strong absorption of trace gases. For any of the six standard atmospheric profiles,
channels are removed if changes in trace gas content induce a BT shift of >1 K. Channels are retained if the gas-induced BT
180   change is <1 K; the influence of these gases is then incorporated into the forward model for simulation. Among nine trace
gases (CH_4, CO, N_2O, CCl_4, CFC-11, CFC-12, CFC-14, HNO_3, NO_2, OCS, and NO), only the first three significantly affect
the channel BT (Collard, 2007). As the absorption bands of CO and N_2O fall outside this study's spectral range, we focus on
CH_4 for testing. Channels significantly influenced by ozone and solar irradiance are also excluded.

The second step involves eliminating channels with excessive noise. To minimize the risk of excluding relevant spectral bands
185   or retaining inappropriate bands, a threshold of 0.2 K for NEdT is adopted as the pre-screening criterion for channel selection.
The third step excludes channels with non-linear Jacobian matrix and multiple Jacobian peaks. Using the LBLRTM model and
six standard atmospheric profiles, we calculate the Jacobian matrix for temperature and water vapor. Channels exhibiting
significant double or multiple peaks in the Jacobian matrix are excluded. Figure 2 illustrates the channels rejected during pre-
screening: the red areas indicate channels influenced by O_3, purple areas are those affected by CH_4, and yellow areas those
190   with multiple peaks in the Jacobian matrix.

**Figure 2: FY-3E/HIRS-II channel pre-screening results: red and purple highlight channels affected by O_3
and CH_4, respectively; yellow highlights channels with multiple peaks in the Jacobian matrix.**

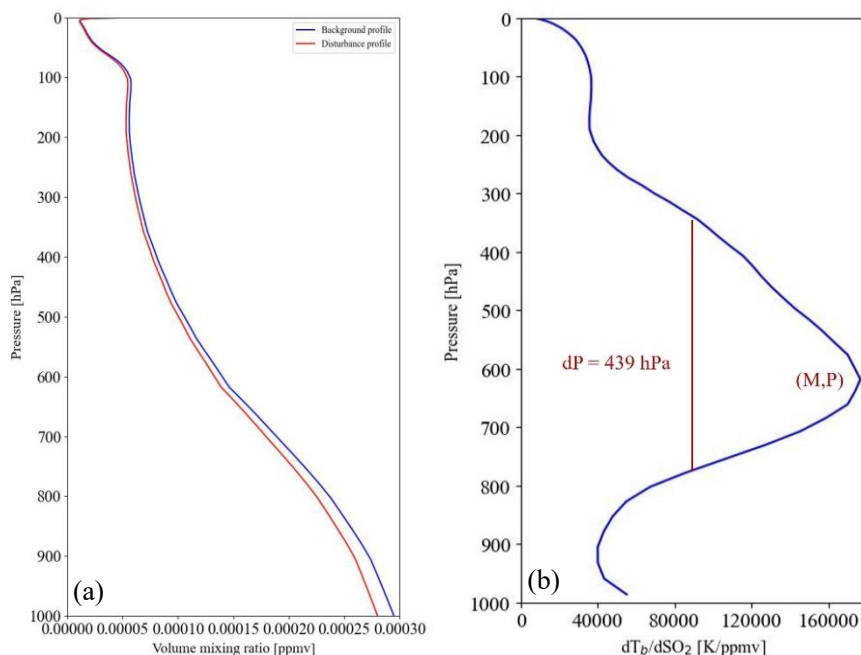## 3.2 Jacobian matrix based information analysis

We calculate and analyze the information generated by water vapor, temperature, and SO_2 at different altitudes to select and utilize the most relevant channels. To evaluate the capability of HIRAS-II channels to provide information on these parameters, we employ the Jacobian matrix for channel selection. The Jacobian functions can identify a set of optimal channels with maximum or minimum information content for each atmospheric profile. It assesses the sensitivity of radiation to the specific physical and chemical parameters. For a specified wavenumber (v), the sensitivity of BT to variations in geophysical parameters (X) is represented by the Jacobian matrix for each pressure layer (Coopmann et al., 2020) as follows:

$$J_v(X) = \frac{\partial BT(v)}{\partial X},\qquad(2)$$

The Jacobian matrix illustrates the sensitivity of atmospheric BT to temperature, humidity, and various gas concentrations at a given wavenumber (Aires et al., 2016).

Three key parameters for measuring the properties of a Jacobian matrix are employed. The first parameter is the maximum value of each Jacobian matrix, denoted as M, quantifies the information (here, all discussions of M in this paper only consider its maximum value, i.e., $|M|$). The second is the pressure level P corresponds to the height where the Jacobian matrix attains its peak value, indicating the altitude at which the IR radiation is the most responsive to variations in atmospheric composition. The third is the Jacobian matrix peak's full width at half maximum is indicated by the parameter dP, defined as the pressure difference between the two levels where the Jacobian matrix value reaches half of its maximum. This metric represents the vertical extent of the atmospheric layer contributing most significantly to the IR signal. Figure 3 schematically represents the SO_2 profile, the Jacobian peak and the maximum half-width of the Jacobian function under the conditions of the US standard atmosphere, 1976.

Figure 3: Representation of the maximum half-width and peak value of the SO₂ Jacobian function for the US Standard Atmosphere, 1976: (a) SO₂ profile, (b) 1163.125 cm⁻¹ channel.

210   In selecting channels minimally influenced by atmospheric temperature, we prioritize those channels that are primarily sensitive to a single gas with a constant concentration. Consequently, we utilize the spectral absorption region of CO_2 (666 – 1000 cm⁻¹) to calculate the temperature Jacobian matrix and combine this with the atmospheric IR window channel to select the atmospheric temperature channels (Li et al., 2022). The specific channel selection process is shown in Fig. 4, it illustrates the cross-comparison process using the three key parameters of Jacobian matrices in the range of SO_2, water vapor and CO_2

215   absorption region. Initially, we computed the temperature, water vapor, and SO_2 Jacobian matrix for the six standard atmospheric profiles. Then, the similarity in the peak and half-width of the Jacobian matrix at specific pressure level P for HIRAS-II channels in SO_2, water vapor and temperature absorption region were cross-compared. The temperature Jacobian information for the atmospheric temperature channel needs to align with that for the SO_2 channel to minimize the influence of atmospheric water vapor and temperature to SO_2. Similarly, the temperature and water vapor Jacobian information for the

220   water vapor absorption channel must match the corresponding information for the SO_2 channel. Using this information, we then identified the atmospheric temperature channels, water vapor absorption channels, and SO_2-sensitive channels. Considering the variability in the sensitivity of the HIRAS-II channels to the atmospheric conditions, we utilize 1040 hPa as the near-surface atmospheric pressure and compute the Jacobian matrices for water vapor, temperature, and SO_2 across 99 vertical atmospheric sections of the six atmospheric profiles.
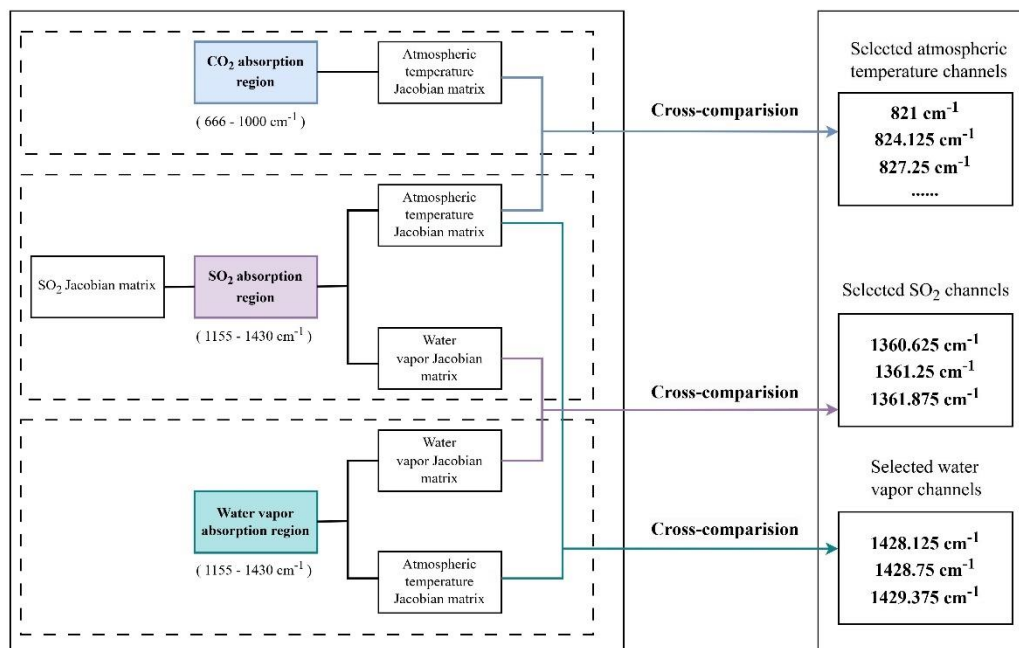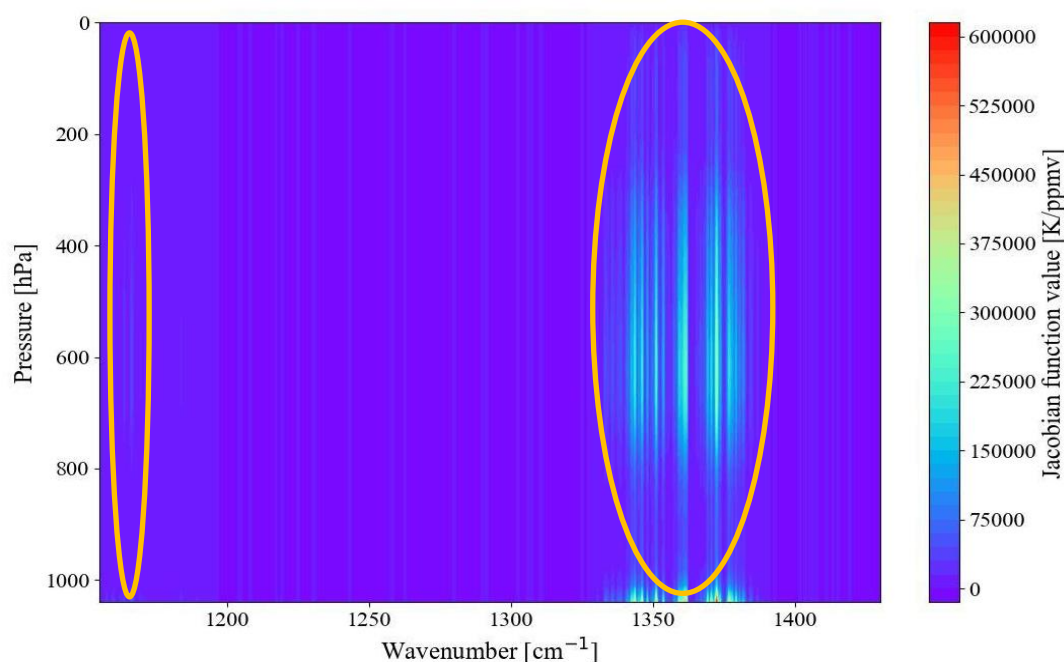
Atmospheric
Measurement
Techniques
Discussions

Figure 4: Schematic diagram of channel selection method.

3.2.1 SO₂ channel selection

For SO₂, we perturb the atmospheric profiles at different pressure levels using a 5% gas content. Given the low SO₂ content under the other five atmospheric conditions, this study focuses on the SO₂ information for the US Standard Atmosphere, 1976. The corresponding SO₂ Jacobian functions (Fig. 5) clearly shows that the SO₂ absorption region is located mainly around the central wavenumbers of 1360 and 1225 cm^{-1}. The SO₂ absorption information content of the 1360 cm^{-1} absorption region is significantly higher than that of the 1225 cm^{-1} absorption region; therefore, we select SO₂-sensitive channels with a central wavenumber around 1360 cm^{-1}. Considering the needs of subsequent retrieval work and the existence of some SO₂ signals near 1225 cm^{-1}, we still conducted a plume sensitivity analysis on the 1225 cm^{-1} channel. In addition, SO₂ absorption information is discernible at various altitudes in the atmosphere, particularly in the middle atmosphere and near the surface. To obtain pure SO₂ absorption information, it is essential to eliminate information about the surface temperature, atmospheric temperature, and water vapor that might interfere with the SO₂ observation channels, thereby avoiding overestimation or misestimation of the SO₂ content and dispersion trends. We selected the top three channels with the highest Jacobian matrix values in the SO₂ absorption region near 1360 cm^{-1}, which are 1360.625 cm^{-1}, 1361.25 cm^{-1} and 1361.875 cm^{-1}. These three channels contain prominent SO₂ absorption information.
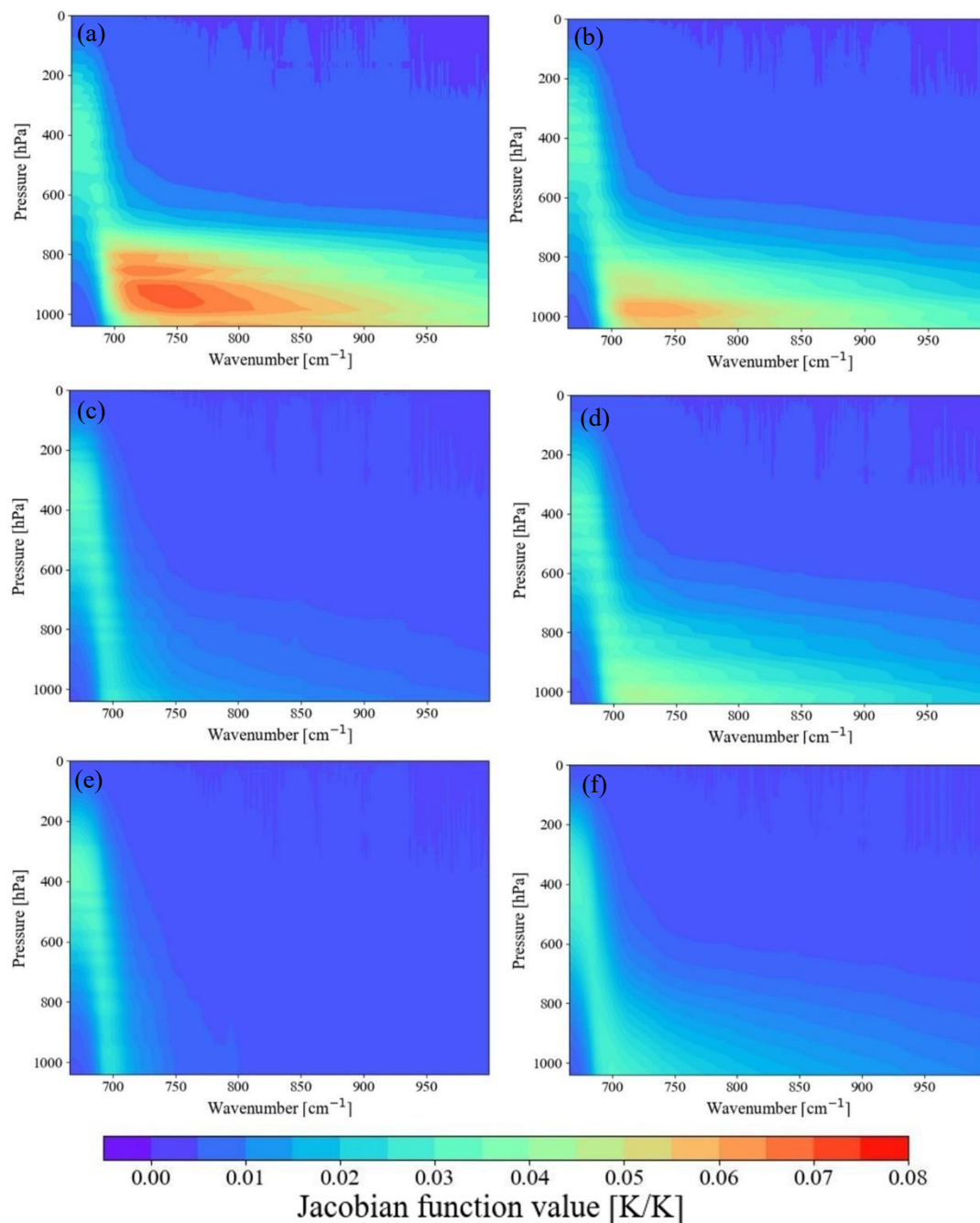
Figure 5: Schematic diagram of the SO₂ Jacobian matrix with atmospheric profiles from the US Standard Atmosphere, 1976.

3.2.2 Atmospheric temperature channel selection

240   Volcanic eruptions typically change the temperature of the stratosphere and troposphere, making it essential to eliminate any interference effect of atmospheric temperature on SO₂ observations (Yang & Schlesinger, 2002). Fig. 6(a)-(f) shows temperature Jacobian functions for the six atmospheric profiles, revealing that near-surface temperatures are more responsive to temperature perturbations in the tropical, mid-latitude summer, subarctic summer, and US Standard Atmosphere, 1976, profiles, while the mid-latitude winter and subarctic winter profiles exhibit greater fluctuations at higher altitudes. For the

245   atmospheric temperature channels, it is crucial that the temperature Jacobian functions peak at the same altitude as those of the SO₂ channels and have similar half-widths of their Jacobian functions. We compare the temperature Jacobian functions of the SO₂ channels with that of the atmospheric temperature absorption region under each set of atmospheric profiles, so that each channel in the atmospheric temperature absorption region can be compared with all channels in the SO₂ absorption region for atmospheric temperature absorption information. First, we filter out channels where both peak at the same altitude. Then

250   we determine the final atmospheric temperature channels using a threshold of the half-width difference being <0.1. Channels meeting these conditions, along with the SO₂ channels, exhibit consistent temperature absorption information and adequately cover the atmospheric temperature channels for the six observed atmospheric conditions. The atmospheric temperature channels we selected also have similar atmospheric temperature absorption information with multiple SO₂ channels at the same
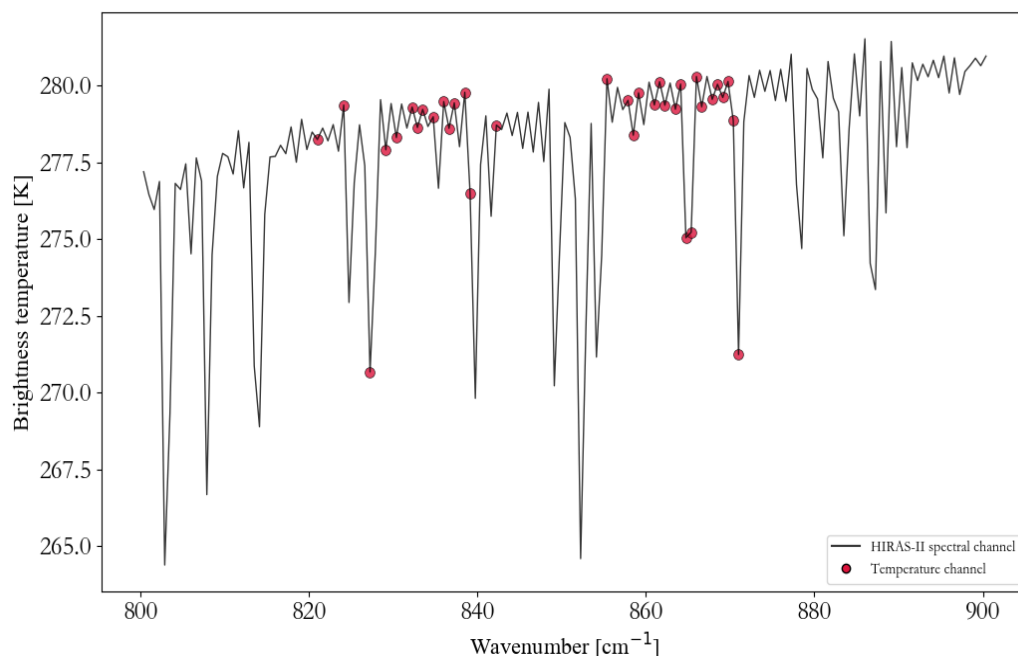
time. Figure 7 shows the specific central wavenumbers of the atmospheric temperature channels and their corresponding BTs

255 under the US Standard Atmosphere, 1976.

Figure 6: Representations of temperature Jacobian functions for the conditions of six atmospheric profiles: (a) tropical atmospheric profile, (b) mid-latitude summer atmospheric profile, (c) mid-latitude

winter atmospheric profile, (d) subarctic summer atmospheric profile, (e) subarctic winter atmospheric profile, and (f) US Standard Atmosphere, 1976.
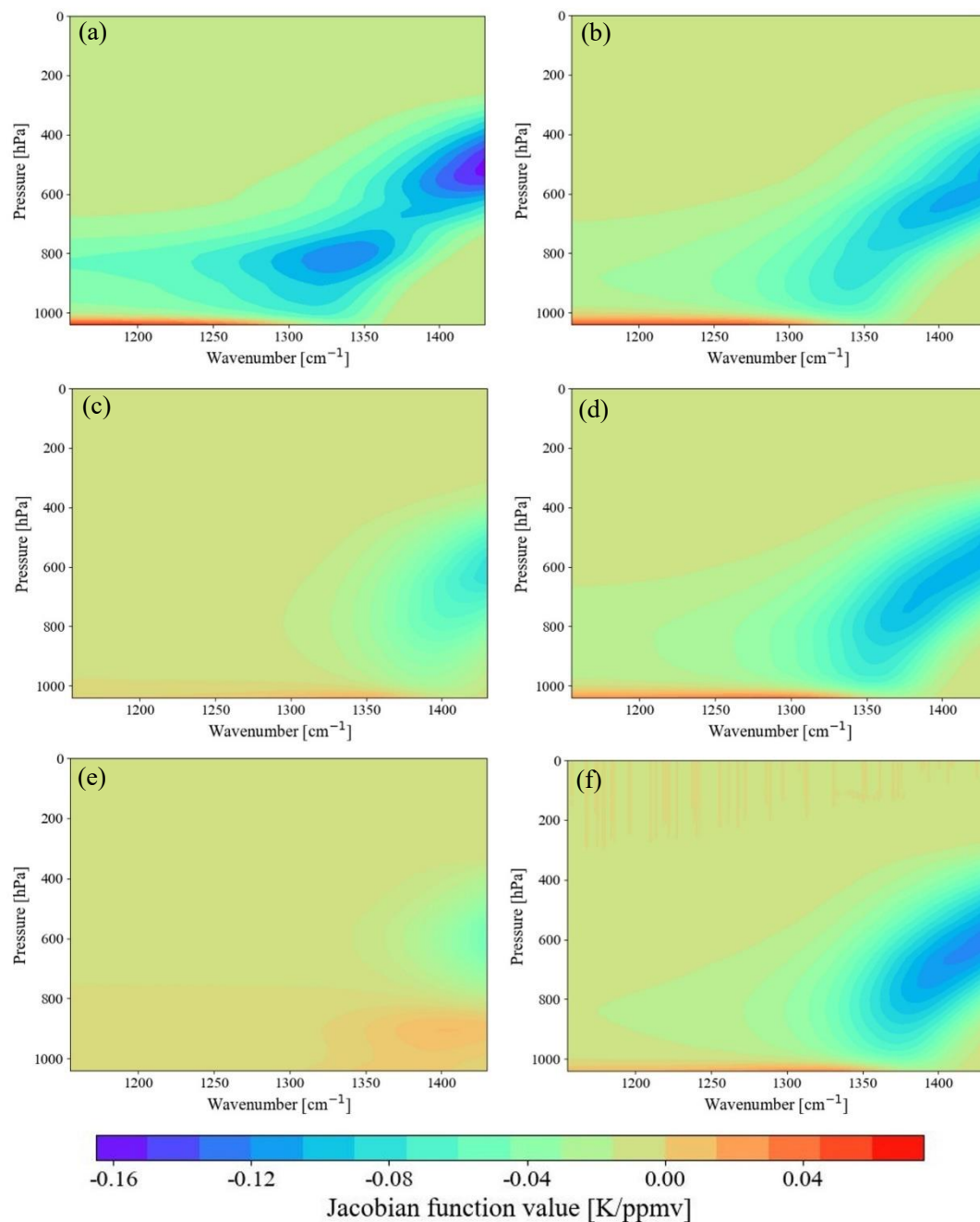

Figure 7: Part of HIRAS-II brightness temperature spectrum with selected atmospheric temperature channels labelled.

3.2.3 Water vapor absorption channel selection

Figure 8 shows strong absorption by water vapor around 1428 cm^{-1} under the six atmospheric conditions, indicating this region contains substantial absorption information on water vapor. In addition, the absolute value of the Jacobian function for water vapor in the lower and middle layers of the 1428 cm^{-1} band can reach up to 0.15 K/ppmv under the tropical, mid-latitude

260   summer, subarctic summer, and 1976 US Standard Atmosphere profiles, indicating that water vapor has a stronger influence than in the mid-latitude winter and subarctic winter profiles. At the same time, it can be seen from Fig. 8 that the SO_2 absorption region around 1360 cm^{-1} is more susceptible to water vapor contamination than the 1225 cm^{-1} absorption region. We calculate the temperature Jacobian functions and water vapor Jacobian functions separately within the water vapor absorption region and SO_2 absorption region. The Jacobian information of water vapor in SO_2 and water vapor absorption region are cross

265   compared. The Jacobian information of atmospheric temperature in SO_2, water vapor absorption region and selected atmospheric temperature channels are also cross compared and the channels with consistent maximum peak value and half-width were selected to ensure that the vertical changes of water vapor and atmospheric temperature were consistent with those of SO_2. The cross-comparison criteria of the Jacobian matrix here are consistent with the selection criteria and threshold of the atmospheric temperature channels in section 3.2.2. Through the cross-comparison process, the selected water vapor channels
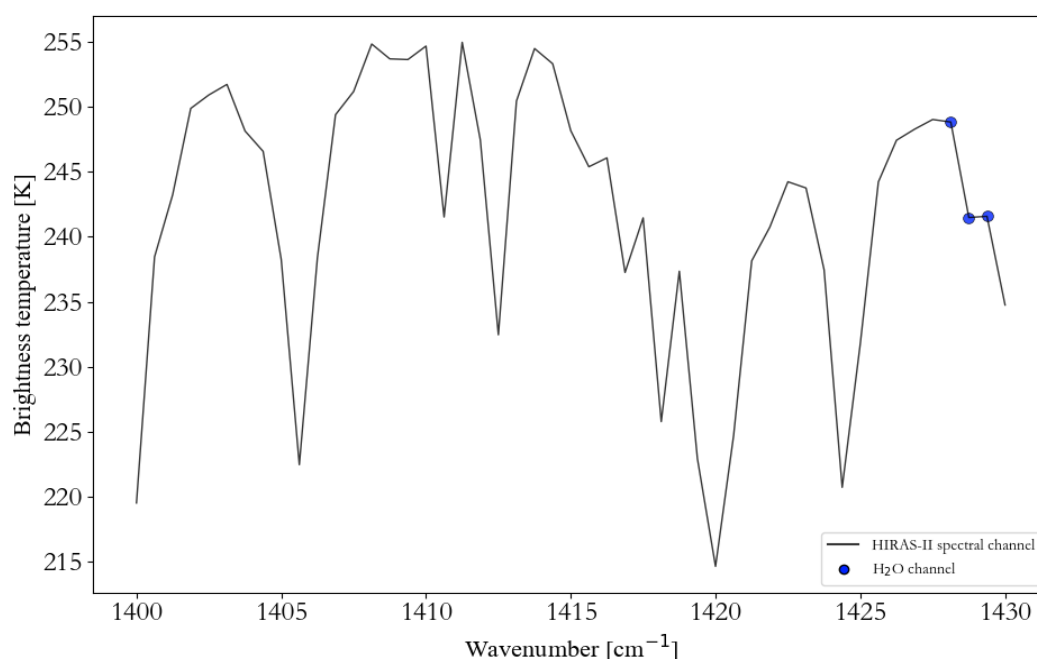
270   can simultaneously contain consistent atmospheric temperature and water vapor absorption information to the SO_2 channels. In this way, the atmospheric temperature and water vapor absorption information carried in the selected SO_2 channels can be removed in the subsequent calculation of the BT difference between the SO_2 channels and the water vapor channels. Figure 9 illustrates the specific central wavenumbers of the selected water vapor absorption channels and their corresponding BTs under the 1976 US Standard Atmosphere.

Figure 8: Representations of water vapor Jacobian functions for conditions of six atmospheric profiles: (a) tropical atmospheric profile, (b) mid-latitude summer atmospheric profile, (c) mid-latitude winter atmospheric profile, (d) subarctic summer atmospheric profile, (e) subarctic winter atmospheric profile, and (f) US Standard Atmosphere, 1976.
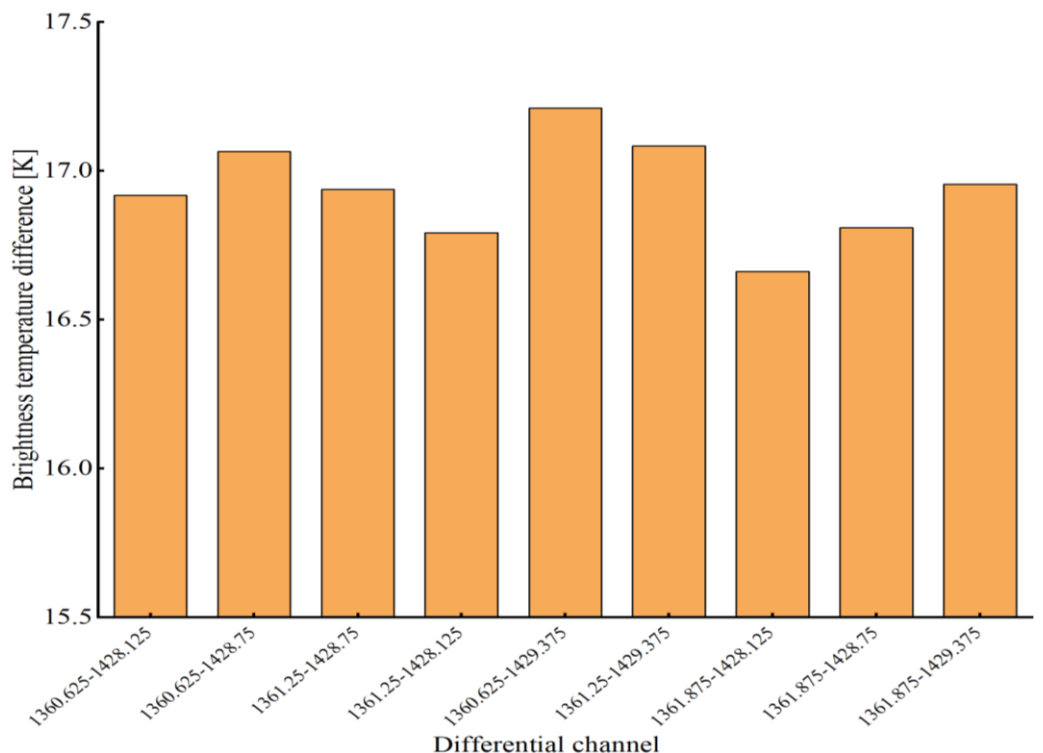
Figure 9: Part of the HIRAS-II brightness temperature spectrum with selected water vapor absorption channels labeled.

275   Under the same SO_2 and water vapor conditions, we selected three groups of SO_2 channels and water vapor absorption channels whose channel combination with the largest brightness temperature difference. By analyzing the BT difference, we determined the SO_2 sensitive channels to accurately carry out the SO_2 retrieval. As can be seen in Fig. 10, 1360.625 cm^{-1} is used as the SO_2-sensitive channel and 1429.375 cm^{-1} as the water vapor absorption channel. The combination of the channels we chose can more effectively remove the water vapor information contained in the SO_2-sensitive channel and can also better

280   demonstrate the SO_2 plume after deducting the effect of water vapor, which lays the foundation for the water vapor retrieval in the subsequent inversion process.

Figure 10: Brightness temperature difference between SO₂ channel and water vapor absorption channel with atmospheric profiles from the 1976 US Standard Atmosphere.

3.3 Surface temperature channel selection

Land surface temperature (or surface skin temperature) is a key variable in IR data inversion (Jimenez-Munoz et al., 2009).
285 The atmosphere minimally reflects, scatters, and absorbs electromagnetic waves in the atmospheric IR window band (Senf & Deneke, 2017). Therefore, we select the clean channel from this range with the highest BT: its use in subsequent analyses as the land surface temperature channels mitigates the influence of land on SO₂ observations. Table 2 presents the distribution of the three channels with the highest BT across the six atmospheric profiles. Notably, the land surface temperature channels for the mid-latitude winter and subarctic winter situations are identical, while those for the mid-latitude summer and subarctic
290 summer profiles are somewhat similar. The tropical atmosphere profile has a land surface temperature channel with a higher wavenumber and shorter wavelength compared with the other profiles. The land surface temperature channel for the US Standard Atmosphere, 1976, falls between those of the other profiles. To ensure the selected land surface temperature channels are applicable to most atmospheric conditions, we identify the two channels with the highest frequency (902.5 and 901.875 cm^{-1}) for subsequent work.

295

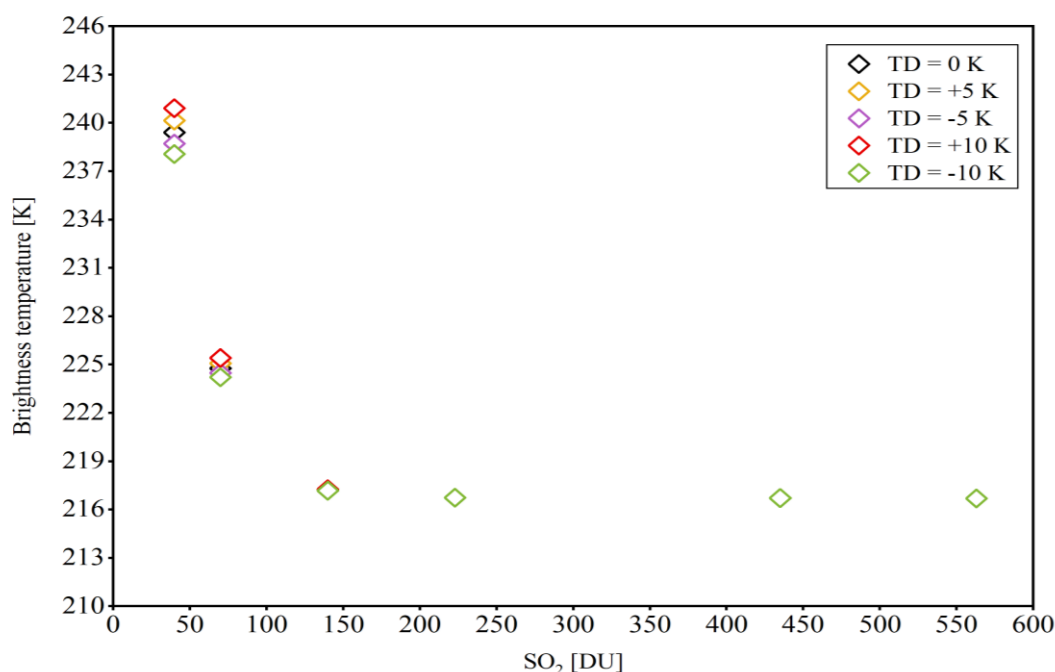Table 2 Distribution of surface temperature channels under six atmospheric profiles

Atmosphere profile	Channel wavenumber (cm^{-1})		
Tropical	916.875	905.625	906.875
Midlat Summer	904.375	903.75	902.5
Midlat Winter	901.25	901.875	902.5
Subarctic Summer	904.375	901.875	902.5
Subarctic Winter	901.25	901.875	902.5
US1976	901.25	901.875	902.5

4 Sensitivity analysis

4.1 Effects of differences in surface temperature and near-surface atmospheric temperature on SO$_2$-sensitive channels

300   Given the variations in surface characteristics affecting atmospheric radiation, we analyzed the impact of the generally low temperature difference between the surface and the overlying air on the SO$_2$ Jacobian function. Meanwhile, the $750 - 1200$ cm^{-1} region is highly sensitive to surface features (Clarisse et al., 2010), and the sensitivity of HIRAS-II to SO$_2$ is significantly influenced by the temperature difference (TD) between the surface and the first distinct layer of air (T_p) (Tsuchiya, 1983). We consider three scenarios: $T_s = T_p$ (TD = 0), $T_p > T_s$ (TD > 0), and $T_p < T_s$ (TD < 0). With $\varepsilon = 0.98$ and $P = 212$ hPa, TD was

305   varied from -10 to 10 K in 5 K increments, and infrared radiation was simulated under each set of conditions. Figure 11 illustrates variations in the SO$_2$ plume in selected channels under different TD conditions for the US Standard Atmosphere, 1976. For a plume SO$_2$ content of <150 DU, an increasingly positive TD enhances SO$_2$ detection in the IR band. Conversely, a decrease in TD limits SO$_2$'s contribution to radiation, thereby constraining its IR remote sensing capability. As the plume's SO$_2$ content increases, the impact of TD on SO$_2$ observation diminishes.

310   These findings suggest that favorable TD conditions can enhance the accuracy of SO$_2$ detection and inversion, which is relevant to monitoring air quality. Due to the vertical distribution of gases, near-surface SO$_2$ tends to be underestimated, but a positive TD helps capture the net absorption of near-surface SO$_2$.
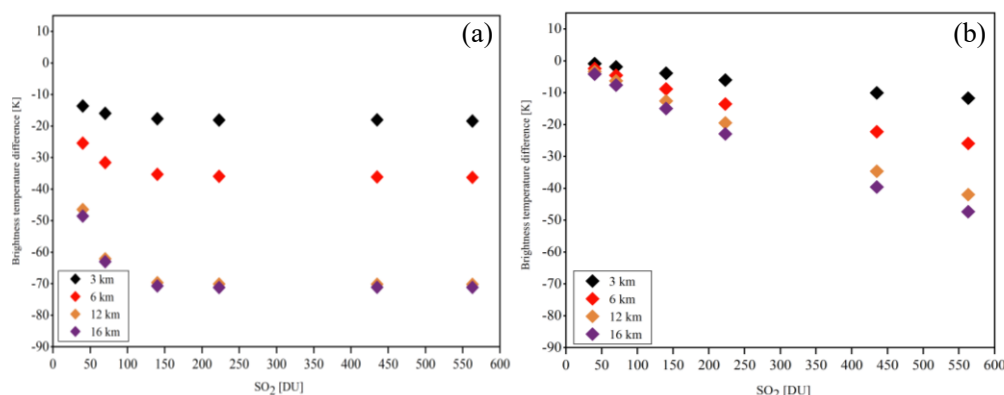
Figure 11: Sensitivity of SO₂ plume measurement to surface temperature with atmospheric profiles from the US Standard Atmosphere, 1976.

4.2 SO₂ plume sensitivity

This study assumes an atmosphere containing SO₂ clouds at various altitudes and simulates the radiative transfer in a standard atmosphere with an introduced SO₂ layer of varying SO₂ concentration. The simulations replicate FY-3E/HIRAS-II's observations of SO₂ volcanic plumes, focusing on the sensitivity of the differences in BT between central wavenumbers of 1360.625 and 902.5 cm⁻¹ and between 1163.125 and 902.5 cm⁻¹ to the total SO₂ column in Dobson units at four plume altitudes (3, 6, 12, and 16 km). The temperature and humidity profiles for these simulations are based on the US Standard Atmosphere, 1976. Figure 12(a) shows that for SO₂ plumes under varying pressure intensities, strong sensitivity is observed when SO₂ content exceeds 50 DU. At 50 ~ 300 DU, the sensitivity of the SO₂ plume increases with altitude. However, beyond 300 DU, the impact of altitude on sensitivity diminishes, indicating a saturation state. Thus, the 1360.625 cm⁻¹ channel is prone to saturation at high SO₂ concentrations. Figure 12(b) shows that for SO₂ plumes below 400 DU, the SO₂ Jacobian function value for the 1163.125 cm⁻¹ channel is relatively low, resulting in reduced sensitivity. Conversely, above 500 DU, the channel exhibits a more pronounced response to increasing SO₂ concentration and plume height.

Therefore, combining these two channels for different SO₂ concentrations enables the representation of a broad range of net SO₂ absorption. The brightness temperature difference between the 1360.625 and 902.5 cm⁻¹ channels can reach up to ~70 K, aligning well with previous experimental results (Ackerman et al., 2008).
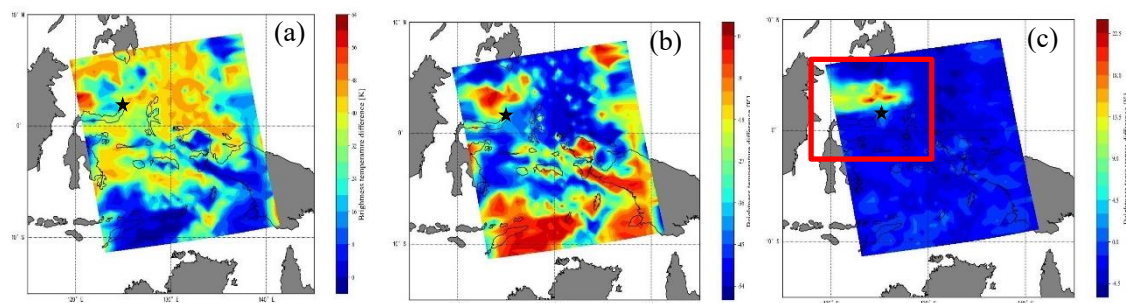
Figure 12: Modeled FY-3E/HIRAS-II brightness temperature differences between the (a) 1360.625 and 902.5 cm^{-1} channels and the (b) 1163.125 and 902.5 cm^{-1} channels for assessing column SO$_2$ content (DU) at four plume heights in atmospheric profiles derived from the US Standard Atmosphere, 1976.

5 Case study

The channels for SO$_2$ detection and retrieval least affected by temperature and water vapor were selected based on experimental results. To verify the accuracy of our channel selection, we compared observations of a volcanic eruption using our selected channels and normal channels.
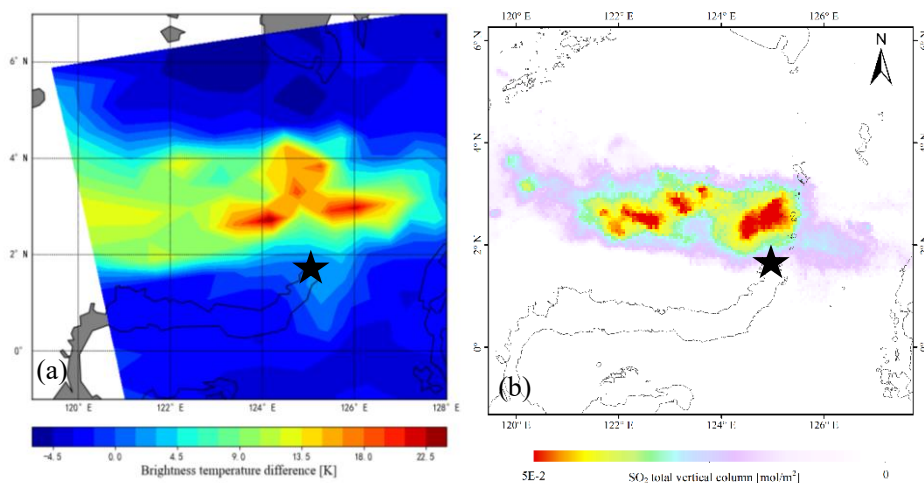
The selected eruption was of Mount Ruang, Indonesia, the southernmost complex volcano in the Sandwich Islands. Its first recorded eruption in 1808 forced the evacuation of over 1,000 people (Galetto et al., 2024). Its violent eruption on the evening of 17 April 2024 was observed by FY-3E/HIRAS-II on 18 April. The collected data are used to explore the advantages of our selected channels.

Figure 13 depicts the differences between the following pairs of channels: 1360.625 and 902.5 cm^{-1}, 1163.125 and 1429.375 cm^{-1}, and 1360.625 and 1429.375 cm^{-1}. Comparison of the first and third difference results indicates that the extent of the SO$_2$ plume near the volcano's center may be overestimated as water vapor due to the background channel's inability to effectively remove the effect of water vapor from the 1360.625 cm^{-1} channel. Water vapor far from the crater is prone to misclassification as SO$_2$ gas. A comparison of the second and third sets of difference results indicates that it is challenging to separate SO$_2$ from the atmosphere due to the smaller value of the SO$_2$ Jacobian matrix for the 1163.125 cm^{-1} channel and its lower sensitivity to SO$_2$ information compared with the 1360.625 cm^{-1} channel. In addition, the eruption increased the atmospheric temperature near the volcano, and the difference between the 1163.125 and 1429.375 cm^{-1} channels cannot remove the atmospheric temperature information observed by the sensors, resulting in significant BT differences over a large area. Figure 13(c) shows the BT difference between the sensitive and background channels based on the experimental selection. The chosen combination of SO$_2$ channels filters out most of the water vapor and atmospheric temperature effects in the observation channel, resulting in better detection of small SO$_2$ plumes.
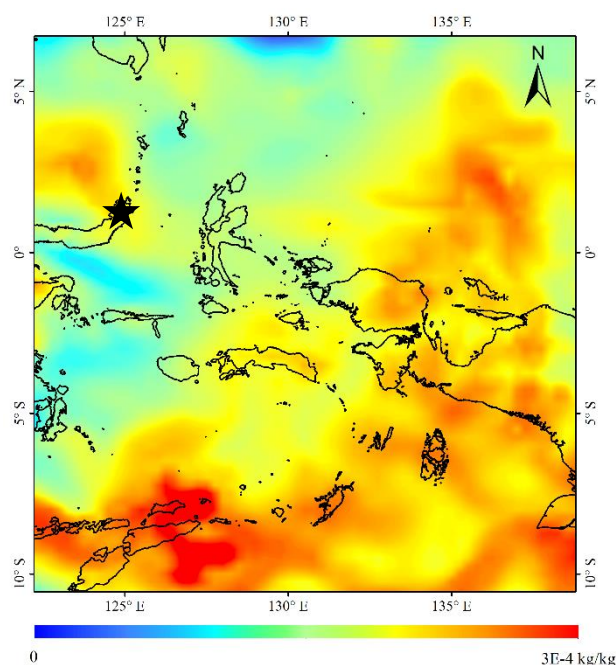
Figure 13: FY-3E/HIRAS-II brightness temperature difference data for the region around Mount Ruang (black star in each image) at 08:55 UT on 18 April 2024 for the channels (a) 1360.625 and 902.5 cm^{-1}, (b) 1163.125 and 1429.375 cm^{-1}, and (c) 1360.625 and 1429.375 cm^{-1}.

Figure 14 compares the FY-3E/HIRAS-II BT difference data (for the area indicated by the red box in Fig. 12(c)) with corresponding observations by Sentinel-5P/TROPOMI. The area of the SO₂ plume's spread and its trajectory are essentially

350 the same for both cases. Figure 15 shows the absolute humidity data at 09:00 UT on 18 April 2024 from the ERA5 atmospheric reanalysis data at an atmospheric pressure of 400 hPa, confirming that the SO₂ plume observed by FY-3E/HIRAS-II in Fig. 13 is largely free of interference by water vapor.

Figure 14: Comparison of SO₂ around Mount Ruang (black star in each image) observed by FY3E/HIRAS-II on 18 April at 08:55 UT and Sentinel-5P/TROPOMI on 18 April at 04:07:08 UT.

Atmospheric
Measurement
Techniques
Discussions

**Figure 15: Absolute humidity data from ERA5 for the area around Mount Ruang (black star) at 09:00
UT on 18 April 2024 at an atmospheric pressure of 400 hPa.**

6 Summary and conclusion

This paper proposes a novel methodology for selecting SO_2 sensitive channels from FY-3E/HIRAS-II hyperspectral IR
atmospheric sensors to quantitatively monitor volcanic SO_2. The peak and maximum half-width of the Jacobian function of
SO_2, temperature and water vapor under different atmospheric conditions were cross compared to identify the optimal channels
for SO_2 detection and retrieval. The results demonstrate that the 1360.625 cm^{-1} channel (wavelength around 7.3 μm) is most
sensitive to SO_2, exhibiting a maximum peak and half width Jacobian values that conveys comprehensive SO_2 absorption
information. While 1163.125 cm^{-1} (wavelength around 8.6 μm) channel has a weaker absorption to SO_2 compared to
1360.625 cm^{-1} channel but also contains valuable information.

Through cross-comparison of the Jacobian matrices of water vapor, temperature and SO_2, it is found that the 1429.375 cm^{-1}
channel (wavelength around 7.0 μm) can not only reflect the water vapor information to the greatest extent, but also maintain
consistent variations with the atmospheric temperature and SO_2, which allows to minimize the influence of atmospheric water
vapor and temperature on SO_2 detection and retrieval. In the atmospheric IR window band, we identify two channels (902.5
and 901.875 cm^{-1}) with the highest frequency of maximum BT under different atmospheric conditions as the land surface
temperature channel to mitigate the influence of land on SO_2 observations.

A sensitivity study shows that the BT difference (BTD) between the experimentally selected SO_2 sensitive channel (1360.625 cm^{-1} channel) and the background channel (902.5 cm^{-1} channel) demonstrates a pronounced relationship to SO_2 at 50 ∼ 300 DU. To address the phenomenon of saturation of the SO_2 response in the 1360.625 cm^{-1} channel at high concentrations, we propose to use the 1163.125 cm^{-1} channel to provide auxiliary information. It is demonstrated that the 1163.125 cm^{-1} channel exhibits a more significant and linear response to increasing SO_2 concentration and plume height when the SO_2 is above 500 DU. In addition, in the lower and middle layers, a positive difference between the surface air temperature and the surface skin temperature enables the IR band to capture more SO_2 information. By further analyzing the BTD between the 1360.625 cm^{-1} and 1429.375 cm^{-1}, the influence of water vapor and atmospheric temperature from 1360.625 cm^{-1} can be effectively removed.

The main advantage of this methodology is that it comprehensively considers the interference of atmospheric temperature, humidity, and surface temperature on SO_2 detection and retrieval, laying the groundwork for developing a more accurate and flexible volcanic SO_2 retrieval algorithm under different atmospheric conditions. Traditional broadband multispectral satellites are seriously influenced by water vapor and atmospheric temperature in SO_2 absorption region, and it is difficult to accurately separate water vapor and temperature information from SO_2 sensitive channels. This methodology overcomes the above problem using satellite-based hyperspectral IR data under a Jacobian Matrix information framework. This method is able to greatly enhance the efficiency for extracting SO_2 information from hyperspectral IR sounder with large number channels while maintain the accuracy. Therefore, it has great potential in both satellite-based and ground-based hyperspectral data processing for volcanic SO_2 retrieval.

For future work, development of a comprehensive dataset representing a variety of volcanic ash spectral properties and atmospheric conditions for SO_2 modeling, detection, and retrieval, is highly desired. Building on the dataset and the traditional line by line forward radiation transfer model, machine learning methods can help explore the nonlinear relationship between volcanic SO_2 and the atmosphere/surface signals from massive forward simulated samples, as well as develop a fast and accuracy radiative transfer model for SO_2 retrieval.

CRediT authorship contribution statement

Xinyu Li: Writing – original draft, Formal analysis, Data curation, Writing – review & editing. **Lin Zhu:** Conceptualization, Methodology, Writing – review & editing. **Hongfu Sun:** Conceptualization, Writing – review & editing. **Jun Li:** Methodology, Writing – review & editing. **Ximing Lv:** Data curation. **Chengli Qi:** Resources. **Huanhuan Yan:** Resources.

Atmospheric
Measurement
Techniques
Discussions

Declaration of competing interest

The authors declare that they have no known competing financial interests or personal relationships that could have appeared to influence the work reported in this paper.

Data availability

Atmosphere profile data are available via https://doi.org/10.5281/zenodo.14174378. TROPOMI SO$_2$ data are freely available via https://doi.org/10.5270/S5P-74eidii. The LBLRTM code are freely available via https://doi.org/10.5281/zenodo.3837549. The ERA5 absolute humidity data are freely available from the Copernicus Climate Change Service (C3S) Climate Data Store (CDS; https://doi.org/10.24381/cds.adbb2d47).

References

Ackerman, S.A., Schreiner, A.J., Schmit, T.J., Woolf, H.M., Li, J.Pavolonis, M.: Using the GOES Sounder to monitor upper level SO$_2$ from volcanic eruptions, J. Geophys. Res., 113, D14S11, doi:https://doi.org/10.1029/2007JD009622, 2008.

Aires, F., Chédin, A., Scott, N.A.Rossow, W.B.: A regularized neural net approach for retrieval of atmospheric and surface temperatures with the IASI instrument, J. Appl. Meteorol., 41, 144-159, doi:10.1175/1520-0450(2002)041<0144:Arnnaf>2.0.Co;2, 2002.

Aires, F., Pellet, V., Prigent, C.Moncet, J.-L.: Dimension reduction of satellite observations for remote sensing. Part 1: A comparison of compression, channel selection and bottleneck channel approaches, Q. J. R. Meteorol. Soc., 142, 2658-2669, doi:https://doi.org/10.1002/qj.2855, 2016.

Bauduin, S., Clarisse, L., Theunissen, M., George, M., Hurtmans, D., Clerbaux, C., et al.: IASI's sensitivity to near-surface carbon monoxide (CO): Theoretical analyses and retrievals on test cases, J. Quant. Spectrosc. Radiat. Transf., 189, 428-440, doi:10.1016/j.jqsrt.2016.12.022, 2017.

Carey, S.Sigurdsson, H.: The 1982 eruptions of El Chichon volcano, Mexico (2): Observations and numerical modelling of tephra-fall distribution, Bulletin of Volcanology, 48, 127-141, doi:10.1007/BF01046547, 1986.

Atmospheric
Measurement
Techniques
Open Access
EGU
Discussions

Carn, S.A., Krueger, A.J., Bluth, G.J.S., Schaefer, S.J., Krotkov, N.A., Watson, I.M., et al.: Volcanic eruption detection by the Total Ozone Mapping Spectrometer (TOMS) instruments: a 22-year record of sulphur dioxide and ash emissions, in: Oppenheimer, C., Pyle, D.M., Barclay, J. (Eds.), Volcanic Degassing. Geological Society of London, p. 0, 2003.

Chang, S., Sheng, Z., Du, H., Ge, W.Zhang, W.: A channel selection method for hyperspectral atmospheric infrared sounders based on layering, Atmos. Meas. Tech., 13, 629-644, doi:10.5194/amt-13-629-2020, 2020.

Clarisse, L., Prata, F., Lacour, J.L., Hurtmans, D., Clerbaux, C.Coheur, P.F.: A correlation method for volcanic ash detection using hyperspectral infrared measurements, Geophys. Res. Lett., 37, 5, doi:10.1029/2010gl044828, 2010.

Clough, S.A., 1994. Radiative transfer model development in support of the Atmospheric Radiation Measurement Program, United States, pp. 11-17.

Cofano, A., Cigna, F., Santamaria Amato, L., Siciliani de Cumis, M.Tapete, D.: Exploiting Sentinel-5P TROPOMI and Ground Sensor Data for the Detection of Volcanic SO_2 Plumes and Activity in 2018–2021 at Stromboli, Italy, Sensors, 21, 6991, 2021.

Collard, A.D.: Selection of IASI channels for use in numerical weather prediction, Q. J. R. Meteorol. Soc., 133, 1977-1991, doi:10.1002/qj.178, 2007.

Coopmann, O., Guidard, V., Fourrié, N., Josse, B.Marécal, V.: Update of Infrared Atmospheric Sounding Interferometer (IASI) channel selection with correlated observation errors for numerical weather prediction (NWP), Atmos. Meas. Tech., 13, 2659-2680, doi:10.5194/amt-13-2659-2020, 2020.

Copernicus Sentinel-5P: TROPOMI Level 2 Sulphur Dioxide Total Column., Version 02, processed by ESA, European Space Agency [data set], https://doi.org/10.5270/S5P-74eidii, 2020.

Corradini, S., Guerrieri, L., Brenot, H., Clarisse, L., Merucci, L., Pardini, F., et al.: Tropospheric Volcanic SO_2 Mass and Flux Retrievals from Satellite, The Etna December 2018 Eruption. 13, 2225, doi: https://doi.org/10.3390/rs13112225, 2021.

Corradini, S., Merucci, L.Prata, A.J.: Retrieval of SO_2 from thermal infrared satellite measurements: correction procedures for the effects of volcanic ash, Atmos. Meas. Tech., 2, 177-191, doi:10.5194/amt-2-177-2009, 2009.

Corradini, S., Merucci, L., Prata, A.J.Piscini, A.: Volcanic ash and SO_2 in the 2008 Kasatochi eruption: Retrievals comparison from different IR satellite sensors, J. Geophys. Res., 115, doi:https://doi.org/10.1029/2009JD013634, 2010.

Crevoisier, C., Chedin, A.Scott, N.A.: AIRS channel selection for CO_2 and other trace-gas retrievals, Q. J. R. Meteorol. Soc., 129, 2719-2740, doi:10.1256/qj.02.180, 2003.

Di, D., Ai, Y.F., Li, J., Shi, W.J.Lu, N.M.: Geostationary satellite-based 6.7 μm band best water vapor information layer analysis over the Tibetan Plateau, J. Geophys. Res.-Atmos., 121, 4600-4613, doi:10.1002/2016jd024867, 2016.

Di, D., Li, J., Han, W.Yin, R.Y.: Geostationary Hyperspectral Infrared Sounder Channel Selection for Capturing Fast-Changing Atmospheric Information, IEEE Trans. Geosci. Remote Sensing, 60, 10, doi:10.1109/tgrs.2021.3078829, 2022.

Doutriaux-Boucher, M.Dubuisson, P.: Detection of volcanic SO_2 by spaceborne infrared radiometers, Atmospheric Research, 92, 69-79, doi:https://doi.org/10.1016/j.atmosres.2008.08.009, 2009.

Atmospheric
Measurement
Techniques
Discussions

Feng, G., Masek, J., Schwaller, M.Hall, F.: On the blending of the Landsat and MODIS surface reflectance: predicting daily Landsat surface reflectance, IEEE Trans. Geosci. Remote Sensing, 44, 2207-2218, doi:10.1109/TGRS.2006.872081, 2006.

Fourrié, N.Rabier, F.: Cloud characteristics and channel selection for IASI radiances in meteorologically sensitive areas, Q. J. R. Meteorol. Soc., 130, 1839-1856, doi:10.1256/qj.03.27, 2004.

Galetto, F., Lillo, D.L.Pritchard, M.: The use of high-resolution satellite topographic data to quantify volcanic activity at Raung volcano (Indonesia) from 2011 to 2021, Research Square[preprint], doi:10.21203/rs.3.rs-4364766/v1, 14 June 2024

Gambacorta, A.Barnet, C.D.: Methodology and Information Content of the NOAA NESDIS Operational Channel Selection for the Cross-Track Infrared Sounder (CrIS), IEEE Trans. Geosci. Remote Sensing, 51, 3207-3216, doi:10.1109/tgrs.2012.2220369, 2013.

Gíslason, S.R., Stefánsdóttir, G., Pfeffer, M.A., Barsotti, S., Jóhannsson, T., Galeczka, I., et al.: Environmental pressure from the 2014-15 eruption of Bardarbunga volcano, Iceland, Geochem. Perspect. Lett., 1, 84-92, doi:10.7185/geochemlet.1509, 2015.

Hersbach, H., Bell, B., Berrisford, P., Hirahara, S., Horányi, A., Muñoz-Sabater, J., et al.: The ERA5 global reanalysis, Q J R Meteorol Soc., 146, 1999-2049, doi:https://doi.org/10.1002/qj.3803, 2020.

Holasek, R.E., Self, S.Woods, A.W.: Satellite observations and interpretation of the 1991 Mount Pinatubo eruption plumes, J. Geophys. Res., 101, 27635-27655, doi:https://doi.org/10.1029/96JB01179, 1996.

Huang, J., Ma, G., Liu, G.Q., Li, J.Zhang, H.: The Evaluation of FY-3E Hyperspectral Infrared Atmospheric Sounder-II Long-Wave Temperature Sounding Channels, Remote Sens., 15, 17, doi:10.3390/rs15235525, 2023.

Inness, A., Ades, M., Balis, D., Efremenko, D., Flemming, J., Hedelt, P., et al.: Evaluating the assimilation of S5P/TROPOMI near real-time SO_2 columns and layer height data into the CAMS integrated forecasting system (CY47R1), based on a case study of the 2019 Raikoke eruption, Geosci. Model Dev., 15, 971-994, doi:10.5194/gmd-15-971-2022, 2022.

Jimenez-Munoz, J.C., Cristobal, J., Sobrino, J.A., Soria, G., Ninyerola, M.Pons, X.: Revision of the Single-Channel Algorithm for Land Surface Temperature Retrieval From Landsat Thermal-Infrared Data, IEEE Trans. Geosci. Remote Sensing, 47, 339-349, doi:10.1109/TGRS.2008.2007125, 2009.

Krueger, A.J., Krotkov, N.A., Yang, K., Carn, S., Vicente, G.Schroeder, W.: Applications of Satellite-Based Sulfur Dioxide Monitoring, IEEE J. Sel. Top. Appl. Earth Observ, Remote Sens., 2, 293-298, doi:10.1109/jstars.2009.2037334, 2009.

Krueger, A.J.Minzner, R.A.: A mid-latitude ozone model for the 1976 U.S. Standard Atmosphere, J. Geophys. Res., 81, 4477-4481, doi:https://doi.org/10.1029/JC081i024p04477, 1976.

Kruse, F.: Predictive subpixel spatial/spectral modeling using fused HSI and MSI data, SPIE, doi: 10.1117/12.542631, 2004.

Kuai, L., Natraj, V., Shia, R.-L., Miller, C.Yung, Y.L.: Channel selection using information content analysis: A case study of CO_2 retrieval from near infrared measurements, Journal of Quantitative Spectroscopy and Radiative Transfer, 111, 1296-1304, doi:https://doi.org/10.1016/j.jqsrt.2010.02.011, 2010.

Li, J.Han, W.: A step forward toward effectively using hyperspectral IR sounding information in NWP, Adv. Atmos. Sci., 34, 1263-1264, doi:10.1007/s00376-017-7167-2, 2017.

Li, J., Menzel, W.P., Schmit, T.J.Schmetz, J.: Applications of Geostationary Hyperspectral Infrared Sounder Observations: Progress, Challenges, and Future Perspectives, Bulletin of the American Meteorological Society, 103, E2733-E2755, doi:https://doi.org/10.1175/BAMS-D-21-0328.1, 2022.

Li, J., Zhou, F.X.Zeng, Q.C.: Simultaneous non-linear retrieval of atmospheric temperature and absorbing constituent profiles from satellite infrared sounder radiances, Adv. Atmos. Sci., 11, 128-138, doi:10.1007/BF02666541, 1994.

Lipton, A.E.: Satellite sounding channel optimization in the microwave spectrum, IEEE Trans. Geosci. Remote Sensing, 41, 761-781, doi:10.1109/tgrs.2003.810926, 2003.

Milstein, A.B.Blackwell, W.J.: Neural network temperature and moisture retrieval algorithm validation for AIRS/AMSU and CrIS/ATMS, J. Geophys. Res.-Atmos., 121, 1414-1430, doi:10.1002/2015jd024008, 2016.

Noh, Y.C., Sohn, B.J., Kim, Y., Joo, S., Bell, W.Saunders, R.: A new Infrared Atmospheric Sounding Interferometer channel selection and assessment of its impact on Met Office NWP forecasts, Adv. Atmos. Sci., 34, 1265-1281, doi:10.1007/s00376-017-6299-8, 2017.

Patrick, M.R., Houghton, B.F., Anderson, K.R., Poland, M.P., Montgomery-Brown, E., Johanson, I., et al.: The cascading origin of the 2018 Klauea eruption and implications for future forecasting, Nat. Commun., 11, 13, doi:10.1038/s41467-020-19190-1, 2020.

Prata, A.J.Kerkmann, J.: Simultaneous retrieval of volcanic ash and SO_2 using MSG-SEVIRI measurements, Geophys. Res. Lett., 34, doi:https://doi.org/10.1029/2006GL028691, 2007.

Prata, A.J., Rose, W.I., Self, S.O'Brien, D.M.: Global, Long-Term Sulphur Dioxide Measurements from TOVS Data: A New Tool for Studying Explosive Volcanism and Climate, in: Volcanism and the Earth's Atmosphere, pp. 75-92, 2004.

Rabier, F., Fourrié, N., Chafaï, D.Prunet, P.: Channel selection methods for Infrared Atmospheric Sounding Interferometer radiances, Q. J. R. Meteorol. Soc., 128, 1011-1027, doi:10.1256/0035900021643638, 2002.

Schmidt, A., Carslaw, K.S., Mann, G.W., Rap, A., Pringle, K.J., Spracklen, D.V., et al.: Importance of tropospheric volcanic aerosol for indirect radiative forcing of climate, Atmos. Chem. Phys., 12, 7321-7339, doi:10.5194/acp-12-7321-2012, 2012.

Seidel, F.C., Kokhanovsky, A.A.Schaepman, M.E.: Fast and simple model for atmospheric radiative transfer, Atmos. Meas. Tech., 3, 1129-1141, doi:10.5194/amt-3-1129-2010, 2010.

Senf, F.Deneke, H.: Uncertainties in synthetic Meteosat SEVIRI infrared brightness temperatures in the presence of cirrus clouds and implications for evaluation of cloud microphysics, Atmospheric Research, 183, 113-129, doi:https://doi.org/10.1016/j.atmosres.2016.08.012, 2017.

Shibata, T.Kinoshita, T.: Volcanic aerosol layer formed in the tropical upper troposphere by the eruption of Mt. Merapi, Java, in November 2010 observed by the spaceborne lidar CALIOP, Atmospheric Research, 168, doi:10.1016/j.atmosres.2015.09.002, 2015.

Taylor, I.A., Preston, J., Carboni, E., Mather, T.A., Grainger, R.G., Theys, N., et al.: Exploring the Utility of IASI for Monitoring Volcanic SO_2 Emissions, Journal of Geophysical Research: Atmospheres, 123, 5588-5606, doi:https://doi.org/10.1002/2017JD027109, 2018.

Tournigand, P.Y., Cigala, V., Lasota, E., Hammouti, M., Clarisse, L., Brenot, H., et al.: A multi-sensor satellite-based archive of the largest SO_2 volcanic eruptions since 2006, Earth Syst. Sci. Data, 12, 3139-3159, doi:10.5194/essd-12-3139-2020, 2020.

Tsuchiya, K.J.A.i.S.R.: Selection of sensors and spectral bands of marine observation satellite (MOS)—1, Advances in Space Research, 3, 257-261, doi:10.1016/0273-1177(83)90128-X, 1983.

Ventress, L.Dudhia, A.: Improving the selection of IASI channels for use in numerical weather prediction, Q. J. R. Meteorol. Soc., 140, 2111-2118, doi:10.1002/qj.2280, 2014.

Watson, I.M., Realmuto, V.J., Rose, W.I., Prata, A.J., Bluth, G.J.S., Gu, Y., et al.: Thermal infrared remote sensing of volcanic emissions using the moderate resolution imaging spectroradiometer, Journal of Volcanology and Geothermal Research, 135, 75-89, doi:https://doi.org/10.1016/j.jvolgeores.2003.12.017, 2004.

Xie, M., Gu, M., Hu, Y., Huang, P., Zhang, C., Yang, T., et al.: A Study on the Retrieval of Ozone Profiles Using FY-3D/HIRAS Infrared Hyperspectral Data, Remote Sens., 15, 1009, doi: https://doi.org/10.3390/rs15041009, 2023.

Yang, F.Schlesinger, M.E.: On the surface and atmospheric temperature changes following the 1991 Pinatubo volcanic eruption: A GCM study, J. Geophys. Res., 107, ACL 8-1-ACL 8-14, doi:https://doi.org/10.1029/2001JD000373, 2002.

Zhang, P., Hu, X., Lu, Q., Zhu, A., Lin, M., Sun, L., et al.: FY-3E: The First Operational Meteorological Satellite Mission in an Early Morning Orbit, Adv. Atmos. Sci., 39, 1-8, doi:10.1007/s00376-021-1304-7, 2022.

540